

Corrosion Performance of Carbon Steel in CO₂ Aqueous Environment Containing Silty Sand with Different Sizes

Songle Lu^{1,2} · Wei Liu¹ · Shian Zhang¹ · Xiaolong Qi¹ · Xiaogang Li¹ · Xuemin Wang²

Received: 12 May 2017 / Revised: 1 August 2017 / Published online: 7 September 2017
© The Chinese Society for Metals and Springer-Verlag GmbH Germany 2017

Abstract Corrosion performance of carbon steel in CO₂ aqueous environment containing silty sand with different sizes was investigated by immersion tests and electrochemical measurements. Silty sand could form an adsorption layer on steel surface in initial period, and the sand adsorption layer was turned into a mixture film of silty sand with corrosion product in last period. The adsorption layer in 325 mesh condition (large size) had the fewest pores for H₂CO₃ transport, exhibiting the highest cathodic current inhibition. In spite of little corrosion product, the sand adsorption film formed in 325 mesh condition induced the lowest corrosion rate. For 1000 and 5000 mesh silty sand, the sand adsorption layer had some pores for H₂CO₃ transport, leading to low cathodic current inhibition and much matrix dissolution. But the adsorption layer for 5000 mesh silty sand (small size) had the largest special surface area to accelerate heterogeneous precipitation of corrosion product FeCO₃. Therefore, the mixture film in 5000 mesh condition was more compact, exhibiting stronger anodic inhibition and lower corrosion rate than those in 1000 mesh condition.

KEY WORDS: Silty sand; Sand adsorption layer; Corrosion product film; Corrosion inhibition; Carbon steel

1 Introduction

Many components and facilities made of carbon steel were exposed to CO₂ aqueous environment and CO₂ corrosion occurred on steel surface [1]. The precipitation of corrosion product FeCO₃ would occur on steel surface or within the pores of a given porous surface film [2]. Usually, the corrosion product could exist as a complete film, which could affect the following corrosion process by changing

electrode reaction area [3, 4]. Many studies indicated that the corrosion product film could be damaged by sand-containing fluid impact, and accordingly, CO₂ corrosion in practical production system was accelerated due to the mechanical damage by sand [5, 6]. But up to now, seldom research was carried out on the effect of sand on CO₂ corrosion process beyond its common mechanical aspect on erosion–corrosion. The clarification of erosion–corrosion mechanism was limited without the sufficient understanding about the effect of sand on the formation of corrosion product film.

Silty sand, the size of which was below 50 μm, could pass through the screen [7–9] and was commonly suspended in practical CO₂ aqueous environment when most of sand with large size was screened [10–13]. Wong et al. performed experimental tests and CFD modeling of silica sand particles erosion in a pipe annular cavity [14]. The results showed that the predicated erosion–corrosion rate in 198-μm particles was in good agreement with experimental values, while that for 38-μm particles was overpredicted.

Available online at <http://link.springer.com/journal/40195>

✉ Wei Liu
weiliu@ustb.edu.cn

¹ Corrosion and Protection Center, Institute for Advanced Materials and Technology, University of Science and Technology Beijing, Beijing 100083, China

² Department of Materials Physics and Chemistry, School of Materials Science and Engineering, University of Science and Technology Beijing, Beijing 100083, China

Mansouri *et al.* also found that the erosion–corrosion results were overpredicted in small particles (25 μm) condition using CFD modeling [15]. These results demonstrated that silty sand might play an important role in the fluid besides its mechanical damage during erosion. Thus, the research on silty sand in the fluid is practically significant in clarifying the effect of sand with small size on corrosion behavior. In our previous research on carbon steel, the single size of silty sand was focused on, and it was found that silty sand could attend the formation of corrosion product film, affecting the surface electrochemical process [16]. Nevertheless, in practical oil and gas production and transportation system, the size of silty sand varied from 0 to 50 μm [9, 17]. The effect of silty sand with different sizes on CO_2 corrosion of carbon steel is still insufficient, which could probably limit the sufficient understanding on CO_2 corrosion process and regularity of carbon steel in practical product environment. Our present research aimed to the above important concern, trying to give further investigation on the effect of the size of silty sand on CO_2 corrosion of carbon steel, which could be beneficial to help the control of practical CO_2 corrosion.

2 Experimental

2.1 Material and Solution

The chemical composition of X70 carbon steel and test solution is shown in Tables 1 and 2. The specimens of 14 mm \times 10 mm \times 5 mm and 10 mm \times 10 mm \times 3 mm were used for immersion tests and electrochemical measurements, respectively. Specimen surface was ground with 360-, 600- and 800-grid SiC abrasive papers in sequence, degreased by acetone, rinsed by alcohol and then dried by cool air. The test solution, which was made up with analytical grade reagents and deionized water, simulated the produced water in an oil field. CO_2 gas was introduced into the solution for 12 h before pouring the solution into the test equipment. Three sizes of silty sand, *i.e.*, 325 mesh (45 μm), 1000 mesh (13 μm) and 5000 mesh (2.6 μm), were used, the composition of which was silicon dioxide.

Table 1 Chemical composition of X70 steel (wt%)

Steel	C	Si	Mn	S	P	Nb	Mo	Ni	Fe
X70	0.055	0.20	1.52	<0.0007	0.008	0.057	0.21	0.22	Bal.

Table 2 Chemical composition of the test solution (mg/L)

Composition	NaCl	Na_2CO_3	NaHCO_3	Na_2SO_4	$\text{MgCl}_2 \cdot 6\text{H}_2\text{O}$	CaCl_2	KCl
Content	543.2	383.6	1022.7	7.1	73.8	49.9	1.8

2.2 Immersion Tests

Figure 1a shows the schematic of immersion test equipment. Specimens were vertically installed in the fixture against the equipment wall. 1 wt% silty sand mixed with the test solution uniformly by magnetic stirrer at the rotating speed of 600 r/min. The immersion test in sand-free condition at the same rotating speed was also performed for comparison. The test temperature was 80 $^\circ\text{C}$, and the immersion duration was 168 h. CO_2 gas was continuously introduced into the solution at atmospheric pressure and the flow rate of 100 mL/min during immersion tests.

At each immersion test, three specimens were used for corrosion mass loss tests and the original weight of each specimen was measured by the electronic analytical balance with an accuracy of 0.1 mg. After the corrosion film on specimen surface was removed using the chemical cleaning procedure, the specimens were rinsed, dried and reweighed to calculate corrosion rate. Two specimens were used for surface and cross-sectional morphology observation of the film by scanning electron microscopy (SEM, JSM-6510) and energy-dispersive X-ray spectrometry (EDS, JSM-6510). The specimens for surface morphology observation were rinsed, dried quickly and kept in the oxygen-free container. The specimens for cross-sectional morphology observation were dried and mounted with epoxy resin. One additional specimen after immersion of 0.5 h was used for nitrogen adsorption–tripping analysis by Quadrasorb SI-MP analyzer (American, Quantachrome). The pore volume, average pore diameter and special surface area of the silty sand layer covered on specimen surface were calculated by QuadraWin software.

2.3 Electrochemical Measurements

Figure 1b shows the schematic of electrochemical measurement equipment. The electrochemical measurements were performed using a conventional three-electrode cell system, where a saturated calomel electrode (SCE) as the reference electrode (RE) and a platinum plate as the counter electrode (CE). The working electrode (WE) was

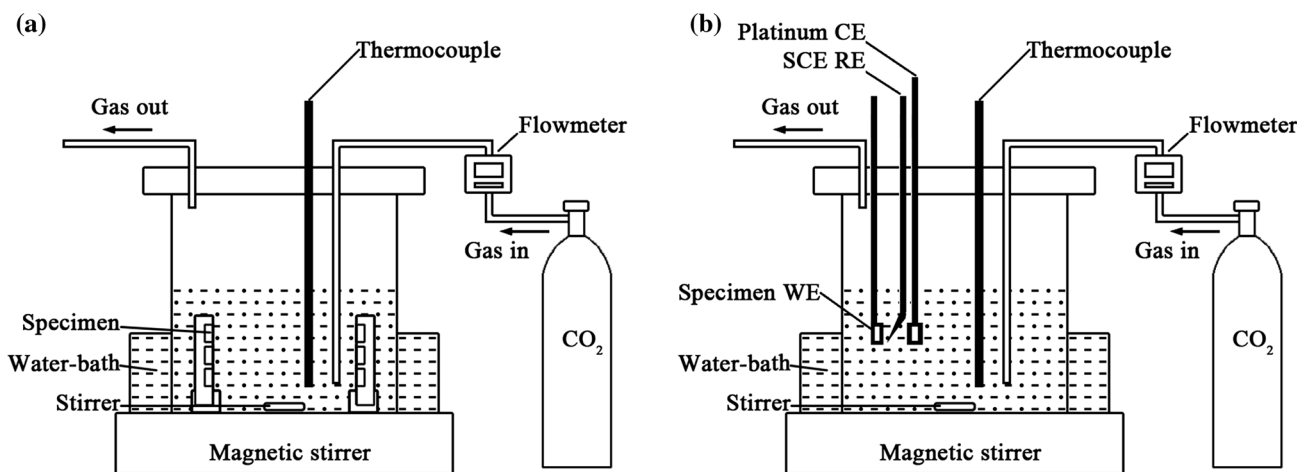


Fig. 1 Schematic of the equipment: **a** immersion test; **b** electrochemical measurement

X70 steel specimen, which was mounted with epoxy resin with only an area of 1 cm^2 exposed to the corrosive environment. The test temperature, rotating speed, pressure and flow rate of CO_2 gas were the same as those for immersion tests. Electrochemical measurements included electrochemical impedance spectroscopy (EIS) and potentiodynamic polarization curves. EIS was measured at OCP with a sinusoidal potential excitation of 5 mV amplitude in the frequency range of 100 kHz to 10 mHz. EIS data were fitted and analyzed by ZSimpWin software. The potential of the potentiodynamic polarization curve measure ranged between $\pm 250 \text{ mV}$ vs. OCP with a scan rate of 1 mV/s .

3 Results

3.1 Corrosion Rate

Figure 2 shows the corrosion rate of X70 steel under different silty sand conditions after immersion of 168 h. The corrosion rates were obviously reduced in all sand-containing conditions compared with that in sand-free condition. Furthermore, in three conditions containing silty sand with different sizes, the corrosion rate in 325 mesh condition was the lowest, and the corrosion rate in 5000 mesh condition was much lower than that in 1000 mesh condition. The results indicated that the size of silty sand obviously affected the corrosion rate of carbon steel in CO_2 aqueous environment.

3.2 Macroscopic Surface Morphology

Figure 3 shows the macroscopic surface morphologies of X70 steel under different silty sand conditions after immersion of 168 h. The specimen surface at sand-free condition was covered with dark film (Fig. 3a), which was

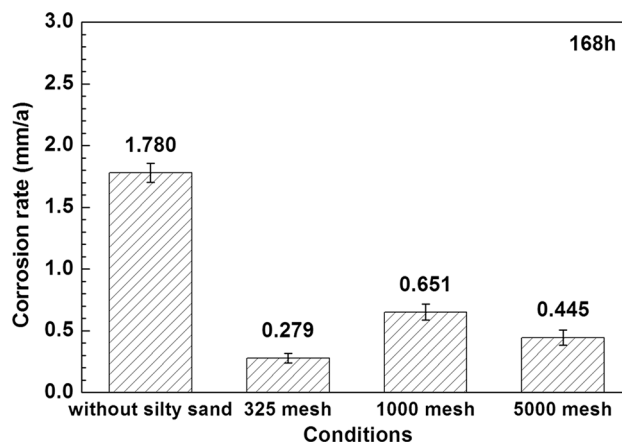


Fig. 2 Corrosion rates of X70 steel under different silty sand conditions after immersion for 168 h

corrosion product film based on previous research [16]. The specimen surface was covered with white film in 325 mesh condition (Fig. 3c). In 1000 and 5000 mesh conditions (Fig. 3e, g), yellow films existed on specimen surface. After removing the film from specimen surface, smooth matrixes were observed in both 325 and 5000 mesh conditions (Fig. 3d, h), which should be attributed to the high protectiveness of the films in these two conditions. But the matrixes were rough in sand-free and 1000 mesh conditions (Fig. 3b, f), indicating that the films properly had low protectiveness in these two conditions.

3.3 Microscopic Surface and Cross-Sectional Morphologies

Figure 4 shows the microscopic surface morphologies and element distributions of the cross-sectional films of X70 steel in different silty sand conditions after immersion of 168 h. Figure 4a, b shows the microscopic morphologies of

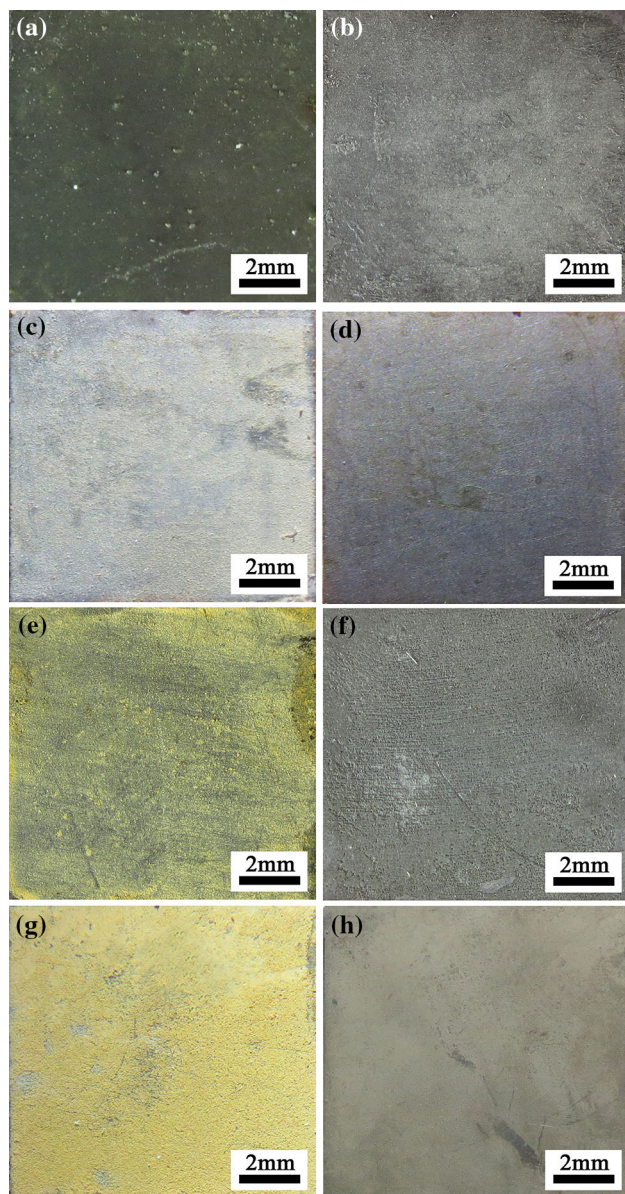


Fig. 3 Macroscopic surface morphologies of X70 steel in different silty sand conditions after immersion for 168 h: **a, b** without silty sand; **c, d** 325 mesh; **e, f** 1000 mesh; **g, h** 5000 mesh

the film on specimen surface formed in sand-free condition. The film was a single-layer structure and all composed of cubic crystals (Point A), and EDS results in Table 3 showed the O/Fe atom ratio of cubic crystals was 3.08. It demonstrated that the cubic crystal was corrosion product FeCO_3 [18–20], which was formed by the precipitation reaction of ferrous ions due to matrix dissolution and carbonate ions in the test solution.

Figure 4c, d shows the microscopic morphologies of the film on specimen surface formed in 325 mesh condition. The film was a porous single layer and composed of irregular particles (Point B) and spherical grains (Point C).

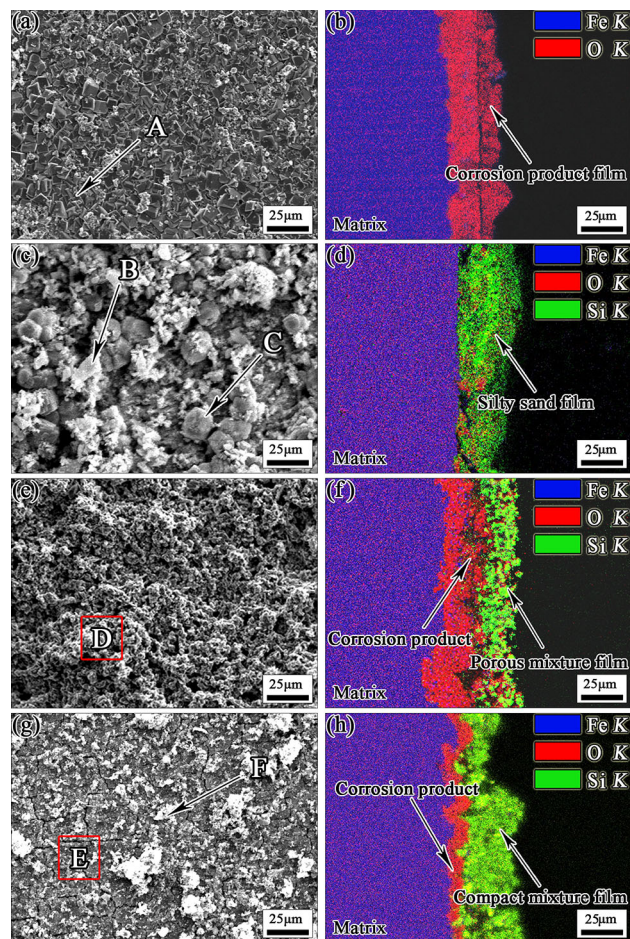


Fig. 4 Microscopic surface morphologies and cross-sectional element distributions of the films of X70 steel in different silty sand conditions after immersion for 168 h: **a, b** without silty sand; **c, d** 325 mesh; **e, f** 1000 mesh; **g, h** 5000 mesh

The elements of the irregular particles were mainly Si of 23.36 at%, O of 68.84 at% and Fe of 7.24 at% (Table 3), indicating that the particles were the mixture of silty sand and small amount of corrosion product FeCO_3 . The spherical grains were also proved to be calcium compound according to its Ca content of 11.77 at% (Table 3), which was formed by the precipitation reaction of calcium ions and anions in the test solution. From the above, the film formed in 325 mesh condition could be considered as a silty sand film mixed with small amount of calcium compound and FeCO_3 and therefore exhibited white in Fig. 3c.

Figure 4e, f shows the microscopic morphologies of the film on specimen surface formed in 1000 mesh condition. The film was a double-layer structure. The outer layer was porous because of the existence of many micropores in Fig. 4e. It was composed of irregular particles (Point D), and the main elements of the particles were Si of 12.62 at%, O of 71.59 at% and Fe of 14.36 at% (Table 3). The result showed that the outer layer was the mixture of

Table 3 EDS analyses on the films of X70 steel after immersion for 168 h (at%)

Condition	Structure		Si	O	Fe	Ca
Without silty sand	Film	Point A	–	73.19	23.73	3.09
325 mesh	Film	Point B	23.36	68.84	7.24	0.55
		Point C	1.32	73.69	13.22	11.77
1000 mesh	Inner layer		1.83	75.55	17.43	5.19
	Outer layer	Point D	12.62	71.59	14.36	1.43
5000 mesh	Inner layer		1.06	74.52	22.95	1.47
	Outer layer	Point E	4.95	73.63	21.42	–
		Point F	21.57	69.56	8.79	0.08

sand with corrosion product FeCO_3 and therefore exhibited yellow in Fig. 3e. The main compositions of the inner layer included Fe and O elements (Table 3), which suggested that it was composed of FeCO_3 [18–20].

Figure 4g, h shows the microscopic morphologies of the film on specimen surface formed in 5000 mesh condition. The film was also a double-layer structure. EDS results in Table 3 illustrated that the outer layer was the mixture of FeCO_3 (Point E) with silty sand (Point F) and the inner layer was mainly composed of FeCO_3 , which were both similar to the film structure in 1000 mesh condition. But different from 1000 mesh condition, no significant micropores could be found on the outer layer in 5000 mesh condition. It demonstrated that the outer layer in 5000 mesh condition was more compact than that in 1000 mesh condition.

The mixture film of silty sand with corrosion product FeCO_3 in 1000 and 5000 mesh conditions had higher protectiveness than the corrosion product film of cubic crystal FeCO_3 formed in sand-free condition, which was related to the compactness of the film [2]. And more compact film formed in 5000 mesh condition resulted in lower corrosion rate than that in 1000 mesh condition. However, the silty sand film with little corrosion product formed in 325 mesh condition was not compact enough but still exhibited high protectiveness, resulting in the lowest corrosion rate. The corrosion inhibition effect of the silty sand film in 325 mesh condition was related to other reason, which will be discussed later.

3.4 Potentiodynamic Polarization Curve

Figure 5 shows the potentiodynamic polarization curves of X70 steel in different silty sand conditions after corrosion time of 168 h. The order of corrosion current densities shown in Table 4 from low to high was 325, 5000, 1000 mesh and sand-free condition, which was consistent with the corrosion rate results from the immersion tests (Fig. 2). In anodic polarization zone, the anodic current densities in three sand-containing conditions were all lower than that in

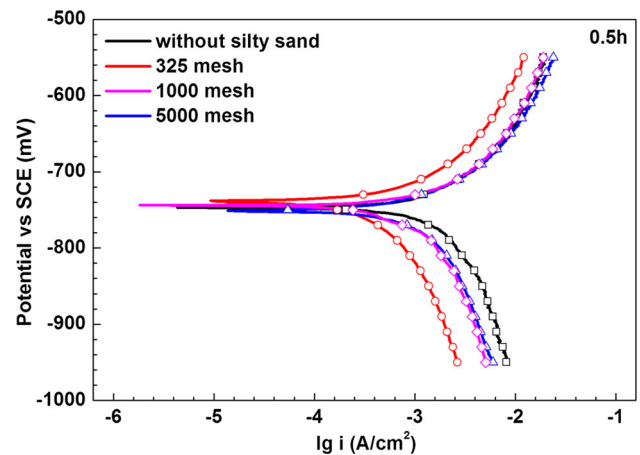


Fig. 5 Potentiodynamic polarization curves of electrochemical specimens of X70 steel in different silty sand conditions after immersion for 168 h

sand-free condition, demonstrating that the films formed at sand-containing conditions exhibited anodic inhibition. Moreover, the order of the anodic current densities from low to high was 5000, 1000 and 325 mesh condition, i.e., anodic inhibition effect increased with reducing size of silty sand. It was widely known that the anodic inhibition effect was closely related to the protectiveness of the film [21, 22]. Thus, it was understandable that the most compact mixture of silty sand with corrosion product in 5000 mesh condition had the highest protectiveness, resulting in the strongest anodic inhibition. And the high anodic current densities in 325 mesh and sand-free conditions were due to the single silty sand film and the single corrosion product film with low protectiveness, respectively.

In cathodic polarization zone, the cathodic current densities in three sand-containing conditions were all lower than that in sand-free condition, demonstrating that the films formed in sand-containing conditions could inhibit cathodic current. However, the order of the cathodic current densities from low to high was 325, 1000 and 5000 mesh, i.e., cathodic current inhibition effect decreased with reducing size of silty sand. Although little corrosion

Table 4 Electrochemical parameters from potentiodynamic polarization curves after 168 h

Condition	E_{corr} versus SCE (mV)	i_{corr} (A cm^{-2})	b_a (mV)	b_c (mV)
Without silty sand	−739	7.341×10^{-6}	37.46	60.12
325 mesh	−737	1.437×10^{-6}	52.66	61.60
1000 mesh	−734	3.184×10^{-6}	57.33	61.39
5000 mesh	−734	1.862×10^{-6}	61.31	64.31

product was formed in 325 mesh condition, the silty sand film still had the strongest cathodic current inhibition. Meanwhile, although the mixture film of silty sand with corrosion product had high compactness and the mixture film in 5000 mesh condition was more compact than that in 1000 mesh condition, cathodic current density was much higher in 5000 mesh condition. It illustrated that silty sand made main contribution on cathodic current inhibition instead of corrosion product. Similar phenomenon was also exhibited in sand-deposited corrosion of carbon steel [23–25]. The deposited sand could act as diffusion barrier, blocking active sites on the electrode surface and reducing cathodic reaction [23].

The above results showed that the film of silty sand with large size in 325 mesh condition had a strong cathodic current inhibition effect, resulting in the lowest corrosion rate of carbon steel. And the mixture film of corrosion product and silty sand with small size in 5000 mesh condition had a strong anodic inhibition effect, resulting in lower corrosion rate of carbon steel than that in 1000 mesh condition.

3.5 Electrochemical Impedance Spectroscopy

Figure 6 shows the EIS plots after corrosion time of 168 h in different silty sand conditions. The Nyquist diagram (Fig. 6a) showed that only one capacitive arc existed in each condition, which was consistent with one time constant indicated by the Bode diagram (Fig. 6b). The EIS electrochemical parameters were quantified by the equivalent circuit shown in Fig. 7, where R_s is solution resistance, R_{ct} is charge transfer resistance and Q_{dl} is constant phase element; this demonstrates the capacitive characteristic of electric double layer. Table 5 gives the electrochemical data fitted from the equivalent circuit. The order of charge transfer resistance R_{ct} from high to low was 325, 5000, 1000 mesh and sand-free condition. Charge transfer resistance R_{ct} reflected the electrode reaction resistance. Thus, the largest R_{ct} at 325 mesh condition illustrated that in spite of little corrosion product, the silty sand film provided high resistance to the electrochemical reaction, which was mainly the cathodic reaction combined with the results in Sect. 3.4 R_{ct} is larger at 5000 mesh condition than that at 1000 mesh condition implying that the compact

mixture film in 5000 mesh condition enhanced high resistance of the electrochemical reaction, which was mainly anodic reaction.

4 Discussion

4.1 Effect of Silty Sand Adsorption Layer on Corrosion Inhibition

In order to prove that silty sand made main contribution on the cathodic current inhibition instead of corrosion product, the immersion tests and electrochemical measurements after corrosion time of 0.5 h were performed. Figure 8 shows the microscopic surface morphologies of specimen surfaces on X70 steel in different silty sand conditions in initial period (0.5 h). Little steel matrix could be dissolved, and therefore, corrosion product could not precipitate on specimen surface. Silty sand absorbed on steel surface due to their tiny size and small mass. Meanwhile, some pores among the sand particles existed in the sand adsorption layer. The amount of pores was related to the size of silty sand. Silty sand with smaller size could form more pores in the same per unit area on specimen surface. Table 6 shows the calculation result of the pore volume in the sand adsorption layer. The total pore volume in the sand adsorption layer increased with reducing size of silty sand.

The potentiodynamic polarization curves of the electrochemical specimens in initial period (0.5 h) could further verified the electrochemical effect of the sand adsorption layer, as shown in Fig. 9. The cathodic current densities were obviously reduced in sand-containing conditions. Moreover, the order of cathodic current densities from low to high was 325, 1000 and 5000 mesh, which was consistent with the result of cathodic current densities after 168 h (Fig. 5). It adequately illustrated that the silty sand adsorption layer provided main contribution on the cathodic current inhibition instead of corrosion product. It could also be inferred that the sand adsorption layer had a blocking effect on the transport of corrosive species to steel surface to attend cathodic reaction.

In CO_2 acid aqueous environment, the cathodic reaction was the direct reduction in H_2CO_3 , as shown in Eqs. (1) and (2) [1, 26–28]:

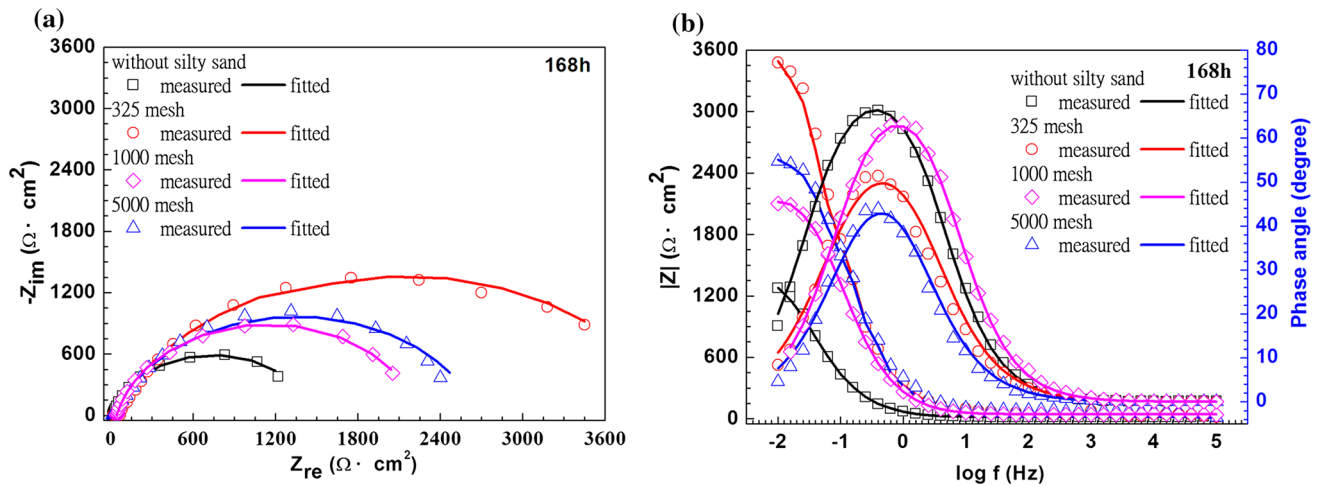


Fig. 6 EIS plots of electrochemical specimens in different silty sand conditions after immersion for 168 h: **a** Nyquist diagram; **b** Bode diagram

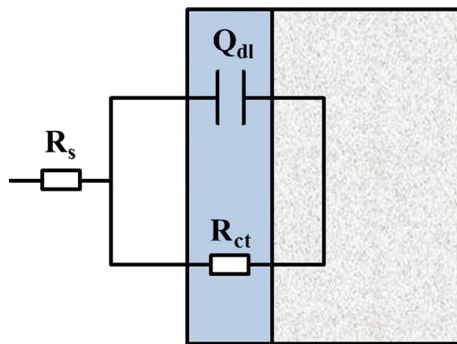


Fig. 7 Electrochemical equivalent circuit for EIS fitting

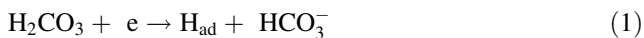


Table 7 shows that the cathodic Tafel slope (b_c) in sand-free condition was 117.62 mV, which was approximate to the Tafel constant of H_2CO_3 reduction (about 120 mV) [29]. Therefore, the reduced cathodic current in sand-containing condition indicated that the adsorption layer of silty sand could block the transport of H_2CO_3 to steel surface. However, the pores existed in the sand adsorption layer could be the transport path of H_2CO_3 . The cathodic current density of H_2CO_3 reduction in 325 mesh condition was the lowest, which reflected the fewest pores in the sand adsorption layer and the highest cathodic current inhibition.

With reducing size of silty sand, the amount of pores in the sand adsorption layer increased. Accordingly, more transport paths of H_2CO_3 to steel surface led to higher cathodic current densities in 1000 and 5000 mesh conditions. The deposited sand environment also exhibited similar cathodic current inhibition. Huang et al. investigated that in CO_2 aqueous environment, the cathodic current density was much lower in glass beads (60 μm) deposited condition than that in SiO_2 powder (44 μm) deposited condition [30]. The deposition porosity of the former was 33%, while that of the latter was 75%. The lower deposition porosity of sand-covered layer reduced more cathodic active sites, exhibiting higher cathodic current inhibition.

In anodic polarization zone, the anodic current density in 325 mesh condition was the lowest. It indicated that the sand adsorption layer with few pores blocked the transport of ferrous ions from matrix surface to the bulk. Deposited sand with large size (200–500 μm) also exhibited this blocking effect [31–33]. The anodic current densities in 1000, 5000 mesh and sand-free conditions were close, which indicated that the sand adsorption layers with more pores in 1000 and 5000 mesh conditions provided enough transport paths for ferrous ions.

In initial period, the sand adsorption layer for 325 mesh exhibited strong electrochemical reaction inhibition, especially in cathodic process. Therefore, little steel matrix was

Table 5 Electrochemical impedance parameters fitted from EIS data

Condition	R_s ($\Omega \text{ cm}^2$)	Q_{dl} ($\Omega^{-1} \text{ s}^n \text{ cm}^{-2}$)	$Q_{dl}-n$	R_{ct} ($\Omega \text{ cm}^2$)
Without silty sand	16.99	3.111×10^{-3}	0.8683	1458
325 mesh	14.17	6.184×10^{-4}	0.7690	3944
1000 mesh	12.97	8.044×10^{-4}	0.8656	2208
5000 mesh	16.02	5.535×10^{-4}	0.7966	2675

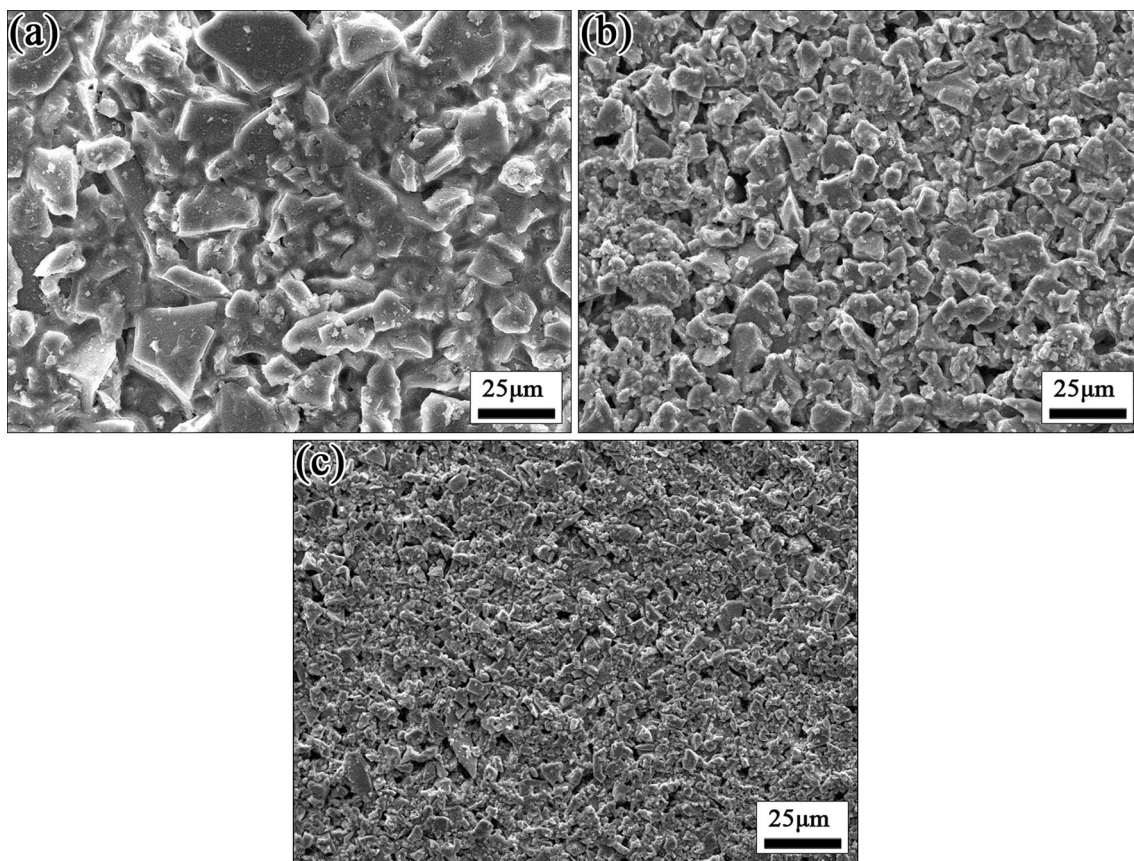


Fig. 8 Adsorption layers of silty sand with different sizes on specimen surfaces of X70 steel (0.5 h): **a** 325 mesh; **b** 1000 mesh; **c** 5000 mesh

Table 6 Pore volume and diameter of the adsorption layers of silty sand with different sizes

Condition	Pore volume (cm ³ /g)	Average pore diameter (nm)
325 mesh	3.966×10^{-3}	12.79
1000 mesh	4.627×10^{-3}	12.91
5000 mesh	6.026×10^{-3}	13.22

dissolved, and accordingly, little corrosion product would precipitate on specimen surface in last period. However, for 1000 and 5000 mesh conditions, due to low cathodic inhibition and no anodic inhibition, much steel matrix was dissolved and corrosion product would precipitate on specimen surface in last period.

4.2 Effect of Mixture Film of Silty Sand with Corrosion Product on Corrosion Inhibition

The steel matrix was dissolved to release Fe²⁺ ions and the precipitation reaction of Fe²⁺ ions and CO₃²⁻ ions occurred, forming corrosion product FeCO₃, as shown in Eqs. (3) and (4) [1]:

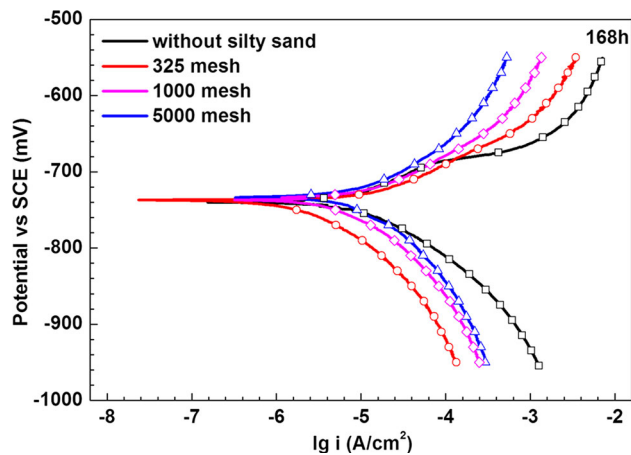


Fig. 9 Effect of adsorption layers of silty sand with different sizes on the cathodic and anodic potentiodynamic polarization curves (0.5 h)



In sand-free condition, FeCO₃ cubic crystals began to heterogeneous nucleate on specimen surface [2] and grew to form crystal corrosion product film (Fig. 4a).

Table 7 Electrochemical parameters from potentiodynamic polarization curves after 0.5 h

Condition	E_{corr} versus SCE (mV)	i_{corr} (A cm^{-2})	b_a (mV)	b_c (mV)
Without silty sand	-747	9.499×10^{-4}	75.19	117.62
325 mesh	-738	1.841×10^{-4}	73.73	92.19
1000 mesh	-744	5.045×10^{-4}	79.28	101.27
5000 mesh	-751	6.095×10^{-4}	77.90	106.12

In sand-containing condition, when corrosion product FeCO_3 was formed after a period of corrosion time, the sand adsorption layer was turned into a mixture film containing silty sand and corrosion product. According to the study by Nešić *et al.* [2], FeCO_3 precipitation could occur on specimen surface and within the sand adsorption layer. The heterogeneous precipitation rate of FeCO_3 could be calculated by two models [34, 35]:

$$R_{\text{FeCO}_3} = A \times e^{54.8 - \frac{123.0 \text{ kJ/mol}}{RT}} \times K_{\text{sp}} \times (S^{1/2} - 1)^2. \tag{5}$$

$$R_{\text{FeCO}_3} = A \times e^{52.4 - \frac{119.8 \text{ kJ/mol}}{RT}} \times K_{\text{sp}} \times (S - 1)(1 - S^{-1}). \tag{6}$$

In these two models, A is the surface area available for precipitation, K_{sp} is the precipitation rate constant, and S is the super-saturation ($S = c_{\text{Fe}^{2+}} c_{\text{CO}_3^{2-}} / K_{\text{sp}}$). In sand-containing condition, A could be considered as the sum of the specimen surface area and special surface area in the sand adsorption layer. The sand adsorption layer with large special surface area could accelerate heterogeneous precipitation of corrosion product and accordingly form compact mixture film within a short immersion time.

Figure 10 shows the multipoint BET (Brunauer–Emmett–Teller) plots of the adsorption layer of silty sand with different sizes in initial period (0.5 h). The BET equation was shown as follows:

$$\frac{1}{W(p_0/p - 1)} = \frac{1}{W_m C} + \frac{C - 1}{W_m C} \cdot \frac{p}{p_0}. \tag{7}$$

where W is the weight of nitrogen adsorbed at a relative pressure, p/p_0 . BET constant C is a magnitude indication of the adsorbent/adsorbate interactions. W_m is the weight of adsorbate constituting a monolayer of surface coverage, which could be obtained from the slope and intercept of the BET plots:

$$\text{Slope} = \frac{C - 1}{W_m C}. \tag{8}$$

$$\text{Intercept} = \frac{1}{W_m C}. \tag{9}$$

Thus, the weight of a monolayer W_m can be obtained by combining Eqs. (8) and (9):

$$W_m = \frac{1}{\text{Slope} + \text{Intercept}}. \tag{10}$$

The special surface area S_t of the adsorption layer of silty sand could be expressed as:

$$S_t = \frac{W_m \cdot N \cdot A_{\text{cs}}}{M} \tag{11}$$

where N is Avogadro’s number ($6.02214145 \times 10^{23}$ molecules/mol), M is the nitrogen molar mass (28.013 g/mol) and A_{cs} is the cross-sectional area for nitrogen ($1.62 \times 10^{-19} \text{ m}^2$).

According to calculation results in Table 8, special surface area in sand adsorption layer increased with reducing size of silty sand. Therefore, in the same corrosive environment, the precipitation rate of FeCO_3 was the fastest in 5000 mesh condition. The mixture of silty sand with corrosion product in 5000 mesh condition became compact preferentially (Fig. 4g) compared with other conditions, which resulted in the lowest anodic current in the potentiodynamic polarization curves after corrosion time of 168 h (Fig. 5).

4.3 Corrosion Inhibition Mechanism Under Different Silty Sand Conditions

From above results, the corrosion rate in CO_2 aqueous environment containing silty sand was dominated by two

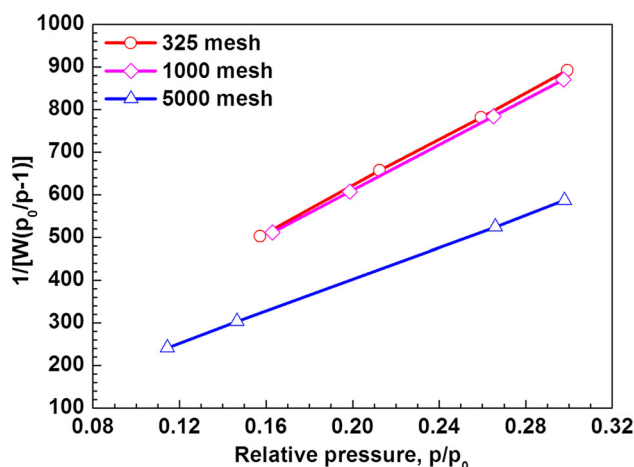
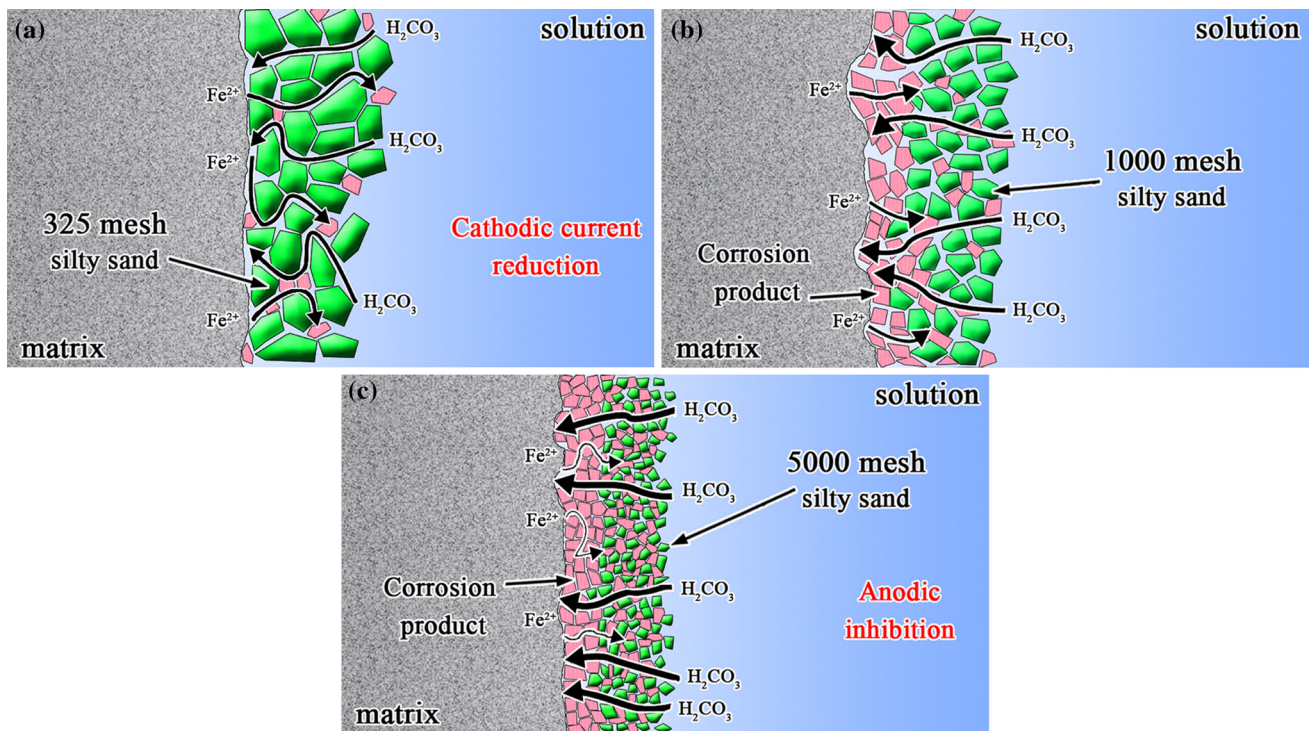


Fig. 10 BET plots of adsorption layers of silty sand with different sizes (0.5 h)

Table 8 Special surface area of the adsorption layers of silty sand with different sizes

Condition	Slope	Intercept	C	W_m	Special surface area (m^2/g)
325 mesh	2732.34	74.34	37.75	3.56×10^{-4}	1.241
1000 mesh	2668.06	77.10	35.61	3.64×10^{-4}	1.269
5000 mesh	1884.96	25.11	76.08	5.24×10^{-4}	1.823

**Fig. 11** Schematics of inhibition mechanism of the films produced on carbon steel surface in different silty sand conditions: **a** 325 mesh; **b** 1000 mesh; **c** 5000 mesh

aspects. One was the silty sand adsorption layer formed in initial period, which determined cathodic current inhibition, and the cathodic inhibition effect decreased with reducing size of silty sand. The other was the mixture film of silty sand and corrosion product formed in last period, which determined anodic inhibition, and the anodic inhibition effect increased with reducing size of silty sand.

Figure 11 shows the corrosion inhibition mechanism of the film formed on carbon steel surface in the conditions containing silty sand with different sizes. In 325 mesh condition (Fig. 11a), only one single silty sand film with small amount of corrosion product existed on steel surface (Fig. 4c, d). The cathodic current was obviously reduced due to few pores for H_2CO_3 transport in the sand adsorption layer (Table 6). Charge transfer resistance R_{ct} in 325 mesh condition was the highest (Table 5) due to the highest inhibition effect on cathodic current, leading to the lowest corrosion rate (Fig. 2) in spite of its low anodic inhibition.

In 1000 mesh condition (Fig. 11b), a double-layer film was formed on steel surface (Fig. 4f). The outer layer was a porous mixture of silty sand and corrosion product (Fig. 4e). The sand adsorption layer formed in initial period had much pores (Table 6), leading to low cathodic current inhibition. Then, the porous mixture film formed in last period exhibited low anodic inhibition. Charge transfer resistance R_{ct} in 1000 mesh condition was lower than those in other two silty sand conditions (Table 5) due to both low cathodic and anodic inhibition effect, leading to high corrosion rate (Fig. 2). But the film formed in 1000 mesh condition still had protectiveness compared with that formed in sand-free condition.

In 5000 mesh condition (Fig. 11c), a double-layer film was formed on steel surface (Fig. 4h). The sand adsorption layer exhibited low cathodic current inhibition due to its pores in initial period (Table 6). However, the sand adsorption layer had the largest special surface area for accelerating heterogeneous precipitation of corrosion

product FeCO_3 . Therefore, the adsorption layer was turned into a compact mixture film (Fig. 4g), leading to high anodic inhibition. The higher anodic inhibition in 5000 mesh condition led to higher charge transfer resistance R_{ct} (Fig. 6 and Table 5) and accordingly, resulting in lower corrosion rate compared with 1000 mesh condition (Fig. 2).

5 Conclusions

Corrosion performance of carbon steel in CO_2 aqueous environment containing 325, 1000 and 5000 mesh silty sand was investigated, respectively. The size of silty sand could affect the corrosion rate of carbon steel due to the sand adsorption layer and the mixture film of silty sand with corrosion product by the following mechanism.

- (1) The sand adsorption layer could block H_2CO_3 transport to attend cathodic reaction, exhibiting cathodic current inhibition. The size of silty sand dominated cathodic inhibition effect by the pore amount in the sand adsorption layer. Cathodic inhibition effect decreased with reducing size of silty sand.
- (2) The sand adsorption layer was turned into a mixture film of silty sand and corrosion product in last period, exhibiting anodic inhibition. The size of silty sand dominated anodic inhibition effect by providing surface area for heterogeneous precipitation of corrosion product FeCO_3 and accordingly, increasing the compactness of the mixture film. Anodic inhibition effect increased with reducing size of silty sand.
- (3) Due to the largest inhibition of cathodic current, the adsorption layer of 325 mesh silty sand exhibited the highest charge transfer resistance R_{ct} and the lowest corrosion rate. The compact mixture film of 5000 mesh silty sand also increased charge transfer resistance R_{ct} due to its high anodic inhibition effect, leading to lower corrosion rate than that in 1000 mesh condition.

Acknowledgement The authors are grateful to the funding support from the National Natural Science Foundation of China (Project No. 51571027) and the National Environmental Corrosion Platform (NECP).

References

- [1] S. Nešić, Corros. Sci. **49**, 4308 (2007)
- [2] S. Nešić, M. Nordsveen, R. Nyborg, A. Stangeland, A mechanistic model for CO_2 corrosion with protective iron carbonate films. Paper presented at NACE CORROSION'2001, Houston, USA, March 2001, p. 40
- [3] J.K. Heuer, J.F. Stubbs, Corros. Sci. **41**, 1231 (1999)
- [4] Z.G. Liu, X.H. Gao, C. Yu, L.X. Du, J.P. Li, P.J. Hao, Acta Metall. Sin. (Engl. Lett.) **28**, 739 (2015)
- [5] A. Neville, C. Wang, Wear **267**, 195 (2009)
- [6] R. Barker, X. Hu, A. Neville, Tribol. Int. **68**, 17 (2013)
- [7] P. Linhardt, G. Ball, AC Corrosion: results from laboratory investigations and from a failure analysis. Paper presented at NACE CORROSION'2006, Houston, USA, March 2006, p. 6160
- [8] S. Lux, M.R. Sustache, C. Marsh, J. Bushman, Dilute flowable backfill for corrosion mitigation of buried steel pipe: experimental procedure. Paper presented at NACE CORROSION'2012, Houston, USA, March 2012, p. 1750
- [9] M. Parsi, K. Najmi, F. Najafifard, S. Hassani, B.S. Mclaury, S.A. Shirazi, J. Nat. Gas. Sci. Eng. **21**, 850 (2014)
- [10] C. Fan, B.S. Mclaury, S.A. Shirazi, E.F. Rybicki, Experimental research of sand erosion in gas dominant flows. Paper presented at NACE CORROSION'2012, Houston, USA, March 2012, p. 1422
- [11] T.C. Chevrot, E. Valentine, D. Cornally, J.M. Dubibe, Sand management of topside facilities and interfiled gas condensate lines of a HP/HT field. Paper presented at NACE CORROSION'2006, Houston, USA, March 2006, p. 6599
- [12] Z.B. Zheng, Y.G. Zheng, X. Zhou, S.Y. He, W.H. Sun, J.Q. Wang, Corros. Sci. **88**, 187 (2014)
- [13] H.X. Guo, B.T. Lu, J.L. Luo, Electrochim. Acta. **51**, 315 (2005)
- [14] C.Y. Wong, C. Solnordal, A. Swallow, J. Wu, Wear **303**, 109 (2013)
- [15] A. Mansouri, H. Arabnejad, S. Karimi, S.A. Shirazi, B.S. Mclaury, Wear **338–339**, 339 (2015)
- [16] W. Liu, J. Dou, S. Lu, P. Zhang, Q. Zhao, Appl. Surf. Sci. **367**, 438 (2016)
- [17] J. Been, R. Given, K.I. Cameron, R.G. Worthingham, Factors affecting the rate and extent of disbondment of FBE coatings. Paper presented at NACE CORROSION'2005, Houston, USA, March 2005, p. 5138
- [18] B. Ingham, M. Ko, G. Kear, P. Kappen, N. Laycock, J.A. Kimpton, D.E. Williams, Corros. Sci. **52**, 3052 (2010)
- [19] D.G. Li, Y.R. Feng, Z.Q. Bai, M.S. Zheng, Appl. Surf. Sci. **253**, 8371 (2007)
- [20] W. Sun, S. Nešić, R.C. Woollam, Corros. Sci. **51**, 1273 (2009)
- [21] F.F. Eliyan, A. Alfantazi, Corros. Sci. **85**, 380 (2014)
- [22] L. Niu, Y.F. Cheng, Appl. Surf. Sci. **253**, 8626 (2007)
- [23] R. Barker, B. Pickles, A. Neville, General corrosion of X65 steel under silica sand deposits in CO_2 -saturated environments in the presence of corrosion inhibitor components. Paper presented at NACE CORROSION'2014, Houston, USA, March 2014, p. 4215
- [24] V. Pandarinathan, K. Leplová, W.V. Bronswijk, Corros. Sci. **85**, 26 (2014)
- [25] J. Huang, B. Brown, S. Nestic, Localized corrosion of mild steel under silica deposits in inhibited aqueous CO_2 solutions. Paper presented at NACE CORROSION'2013, Houston, USA, March 2013, p. 2144
- [26] L.G.S. Gray, B.G. Anderson, M.J. Danysh, P.R. Tremaine, Mechanisms of carbon steel corrosion in brines containing dissolved carbon dioxide at pH 4. Paper presented at NACE CORROSION'1989, Houston, USA, March 1989, p. 464
- [27] L.G.S. Gray, B.G. Anderson, M.J. Danysh, P.R. Tremaine, Effect of pH and temperature on the mechanism of carbon steel corrosion by aqueous carbon dioxide. Paper presented at NACE CORROSION'1990, Houston, USA, March 1990, p. 40
- [28] Y. Ishiguro, K. Fujimura, K. Eguchi, T. Nakahashi, Electrochemical analyses of 15%Cr and 17%Cr martensite-based stainless steel OCTG materials with a possible range of austenite ratio. Paper presented at NACE CORROSION'2016, Houston, USA, March 2016, p. 7474

- [29] C.D. Waard, D.E. Milliams, *Corrosion* **31**, 177 (1975)
- [30] J. Huang, B. Brown, X. Jiang, B. Kinsella, S. Nestic, Internal CO₂ corrosion of mild steel pipelines under inert solid deposits. Paper presented at NACE CORROSION'2010, Houston, USA, March 2010, p. 10379
- [31] G.A. Zhang, N. Yu, L.Y. Yang, X.P. Guo, *Corros. Sci.* **86**, 202 (2014)
- [32] V. Pandarinathan, K. Lepková, W.V. Bronswijk, *Corros. Sci.* **85**, 26 (2014)
- [33] D. Han, R.J. Jiang, Y.F. Cheng, *Electrochim. Acta* **114**, 403 (2013)
- [34] M.L. Johnson, M.B. Tomson, Ferrous carbonate precipitation kinetics and its impact on CO₂ corrosion. Paper presented at NACE CORROSION'1991, Houston, USA, March 1991, p. 268
- [35] E.W.J. Hunnik, B.F.M. Pots, E.L.J.A. Hendriksen, The formation of protective FeCO₃ corrosion product layers in CO₂ corrosion. Paper presented at NACE CORROSION'1996, Houston, USA, March 1996, p. 6